CHEMISTRY OF MATERIALS

pubs.acs.org/cm

Article

Influence of an *N,N,N*-Trimethyl-1-adamantyl Ammonium ($TMAda^+$) Structure Directing Agent on Al Distributions and Pair Features in Chabazite Zeolite

Xiaoyu Wang, Yujia Wang, Ahmad Moini, Rajamani Gounder, Edward J. Maginn, and William F. Schneider*

Cite This: https://doi.org/10.1021/acs.chemmater.2c01465

Read Online

ACCESS | Metrics & More | Article Recommendations | Supporting Information

ABSTRACT: While organic structure directing agents (OSDAs) are well known to have a directional influence on the topology of a crystallizing zeolite, the relationship between OSDA charge and siting of aliovalent ions on a primarily siliceous framework is unclear. Here, we explore the relationship between OSDA orientation, Al^{3+} siting, and lattice energy, taking as a model system CHA zeolite occluded with *N,N,N*-trimethyl-1-adamantyl ammonium ($TMAda^+$) at a Si/Al ratio of 11/1. We use density functional theory calculations to parametrize a fixed-charge classical model describing van der Waals and electrostatic interactions between the framework and OSDA. We enumerate and explore all possible combinations of OSDA orientation and Al location (attending to Löwenstein's rule) within a 36 T-site supercell. We find that interaction energies vary over 60 kJ/double-six-ring-unit (d6r). Further, analysis of configurations reveals that energies are sensitive to Al−Al proximity, such that low energies are associated with Al^{3+} pairs in 8-membered rings and higher energies are associated with Al^{3+} pairs in smaller 6- and 4-membered rings. Comparisons with Al siting inferred from CHA zeolite crystallized with $TMAda^+$ suggest that these computed interaction energies are useful reporters of observed Al siting in CHA synthesized with $TMAda^+$.

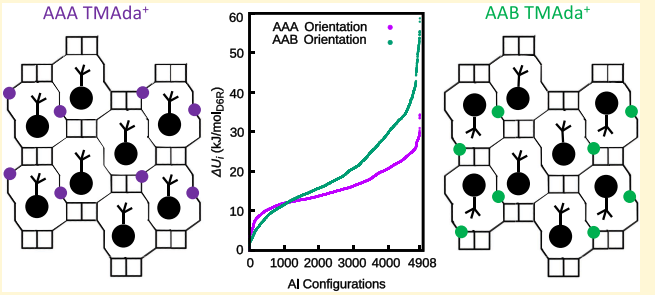

1. INTRODUCTION

Zeolites comprise a large class of microporous and crystalline aluminosilicates constructed primarily of silicon-centered and corner-sharing oxygen tetrahedra.[1] Specific zeolite topologies are often accessed synthetically through cocrystallization of amorphous phases and gels with organic and/or inorganic structure directing agents (SDAs).[2] Organic structure directing agents (OSDAs) are believed to guide zeolites toward particular crystal structures through favorable interactions between the OSDA and the forming framework.[3] The computed interaction energy between a preformed framework and an occluded OSDA has been successfully used as a reporter of the potential for an OSDA to crystallize a particular framework.[4−6] This relationship has been exploited to create new zeolites[7] and to crystallize zeolites with cages tailored to accommodate the transition state of a target reaction.[8,9]

While purely siliceous zeolites are known, the large majority of zeolites contain some amount of aliovalent Al^{3+} substitution onto the Si^{4+} lattice, introducing a net charge onto the zeolite framework. Compensation of that charge by protons generates Brønsted acid sites useful for various hydrocarbon transformations.[10] Further, the relative proximity of those Brønsted sites within a framework can influence chemical and catalytic properties.[11−15] The Al^{3+} centers can also serve as coordination sites for extra lattice metal ions.[16,17] Here too, the proximity of centers can have an influence on metal ion speciation, nuclearity, and reactivity.[18−23]

Experimental evidence indicates that OSDA choice and synthesis conditions can influence the Al^{3+} siting preferences in zeolites.[24] In zeolites that possess more than one type of a symmetry-distinct tetrahedral (T-)site, those conditions can bias Al^{3+} away from or toward particular T-site types, for instance in MFI,[25−28] FER,[29−32] and ITR.[33] These effects can be rationalized based on the relative access of charge-compensating ions during the synthesis to T-sites of distinct environment. On frameworks constructed from a single symmetry-distinct T-site, such as CHA, these influences are manifested in differences in the proximity of Al^{3+} sites.[34−38] CHA is formed from ABC stackings of double-six-ring (d6r) secondary building units and can be crystallized with *N,N,N*-

Received: May 15, 2022
Revised: November 9, 2022

trimethyl-1-adamantyl ammonium ($TMAda^+$) OSDA.[39] CHA zeolites crystallized solely with $TMAda^+$ and at short crystallization times (2 days) are observed to uptake Co^{2+}, but materials prepared at longer crystallization times exhibit no Co^{2+} uptake capacity and to exchange Cu^{2+} only in its monovalent, $CuOH^+$ form.[34,38] These observations indicate that the framework evolves away from six-membered rings (6MRs) containing two Al^{3+} with increasing crystallization time, consistent with a thermodynamic preference against 6MR Al pairs. In contrast, synthesis with Na^+ as a secondary, inorganic SDA results in an enrichment in these Al−Al pair features in the 6MRs.[34,38] Vibrational spectroscopy provides independent verification of these differences.[11] Synthesis with the larger K^+ cation as the secondary SDA again results in CHA zeolites that lack the 6MR Al−Al pair feature.[36]

Charge compensation thus has a determining effect on Al^{3+} siting in CHA. Density functional theory (DFT) calculations show that the proximity-dependent energy of an Al^{3+} pair depends sensitively on the identities of the charge-compensating ions.[40−42] Energy is a decreasing function of Al−Al separation in the Brønsted form[40,41] and exhibits minima at other separations in the presence of mono- (Na^+)[40] or divalent (Cu^{2+})[41] cations. The oblong $TMAda^+$ OSDA is found to occupy the CHA cage in alignment with the long axis; further, the energy of an Al^{3+} charge-compensated by $TMAda^+$ is a strong function of the separation between Al^{3+} and the charged end of the OSDA, reflecting the underlying electrostatic interactions, an effect that is screened but not altered with the inclusion of implicit water.[43] First-nearest-neighbor Al−O−Al linkages become high in energy when charge compensation by $TMAda^+$, in models that exclude or incorporate explicit water,[42] rationalizing the experimentally observed "Löwenstein's rule".[44] Computational comparisons of Al configurations in which $TMAda^+$-alone are occluded within CHA are consistent with an energy bias against 6MR Al−Al pairs.[38] Calculations in which $TMAda^+$ and Na^+ or K^+ are co-occluded within the same CHA cage are consistent, with the former pair resulting in an enrichment in 6MR Al−Al pairs,[36,45,46] while the latter promotes Al−Al pairs at greater separation.[36] The available evidence indicates that computed energies do report on experimentally observed Al siting, independent of the inclusion of H_2O in those models.

These results highlight the potential to use the relationship between OSDA-only occlusion, Al siting and proximity, and energies to report on Al siting over a larger Al- and OSDA configuration spaces. While DFT calculations, in principle, can provide reliable energy predictions, they are, in general, too expensive to be used to explore over a wide configuration space of Al^{3+} and OSDA locations. Classical forcefields, however, can be evaluated rapidly and are well suited to capturing the nonbonded and electrostatic interactions most important to the relative energies of Al^{3+} distributions in a field of OSDAs. To explore this approach, we focus here on the CHA/$TMAda^+$ system. As shown in the schematic representation in Figure 1, this system has the advantages of a single, symmetry-distinct T-site and an OSDA that can orient in only one of two equivalent directions within the zeolite cage.[43] We start with the Dreiding force field[47] successfully applied to neutral analogs of OSDAs[4,6] and augment with charges derived from DFT calculations. We enumerate and explore all possible combinations of OSDA orientation and Al location (attending to Löwenstein's rule) within a 36 T-site supercell. We find that interaction energies vary over 60 kJ/double-six-ring-unit (d6r).

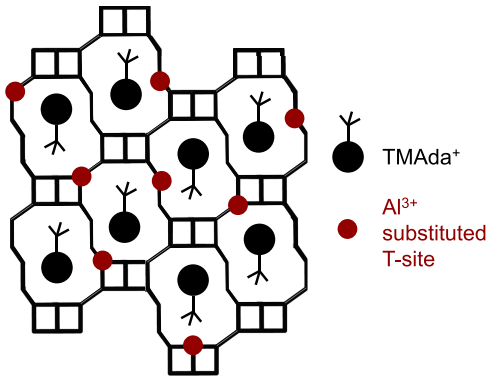

Figure 1. Schematic representation of the CHA/$TMAda^+$ system. Nodes represent Si^{4+} T-sites, lines denote bridging oxygen, and red dots denote Al^{3+} substitutions. Adamantyl body and quaternary nitrogen centers of $TMAda^+$ are represented as black spheres and lines, respectively.

Further, the analysis of configurations reveals that energies are sensitive to Al−Al proximity, such that low energies are associated with Al^{3+} pairs in 8-membered rings and higher energies are associated with Al^{3+} in smaller 6- and 4-membered rings. Comparisons with Al siting inferred from CHA zeolite crystallized with $TMAda^+$ suggest that these computed interaction energies are useful reporters of Al siting.

2. METHODS

2.1. DFT and Ab Initio Molecular Dynamics (AIMD) Simulations. DFT simulations were performed on 36 T-site supercells of varying Al configurations and $TMAda^+$ orientations using the Vienna Ab initio simulation package (VASP), version 5.4.1.[48] Lattice constants were obtained from the Database of Zeolite Structures.[49] Core−valence interactions were treated using the projector-augmented wave (PAW),[50,51] exchange and correlation treated within the Perdew−Burke−Ernzerhof (PBE) generalized gradient approximation (GGA),[52] and the DFT model augmented with the D3 method to describe van der Waals interactions.[53] Plane waves were included to a 400 eV cutoff and the first Brillouin zone sampled at the γ point only. Energies and forces for structures used to parameterize the charge model were converged to 1×10^{-6} eV and 0.03 eV/Å, respectively (CONTCARs included in the Supporting Information). Single-point calculations were performed on the relaxed structures to generate AECCAR0, AECCAR2, and CHGCAR files required for performing subsequent atomic population analysis.[54]

Ab initio molecular dynamics (AIMD) simulations were performed at 633 K in the canonical (NVT) ensemble, using a Nosé−Hoover thermostat with a Nosé mass-parameter (SMASS) of 0.01. A 1 fs time step was used, and hydrogen atoms were replaced by deuterium to accommodate a longer time step. Zeolite framework atoms (Si, Al, and O) were fixed at positions used in the classical simulations described below during the AIMD simulations to facilitate comparisons with the classical models. At each step, self-consistent-field (SCF) electronic energies were converged to 1×10^{-5} eV. Dynamics simulations were run for 10 ps for each configuration. The first 2.5 ps of the trajectory was discarded, and the remaining 7.5 ps was used to calculate the average potential energy.

2.2. Classical Force Field Parameterization. We used the Dreiding force field,[47] previously shown to provide good predictions for interactions between OSDAs and siliceous zeolite frameworks,[4,6] to describe $TMAda^+$ and its van der Waals interactions with the silica−alumina CHA frameworks considered here. We treated $TMAda^+$ as flexible and the CHA framework as rigid. Lattice constants and framework atom positions were fixed at those from the Database of Zeolite Structures.[49]

https://doi.org/10.1021/acs.chemmater.2c01465
Chem. Mater. XXXX, XXX, XXX−XXX

We augmented the Dreiding model with fixed partial charges on TMAda$^+$ and framework atoms to capture electrostatic interactions. To derive the partial charges, we choose three arbitrary initial 36 T-site structures and three occluded TMAda$^+$, relaxed the structures, and used the density-derived electrostatic and chemical (DDEC) approach[55−57] to extract atomic net charges. XYZ files containing raw partial charges obtained from the different minimizations are provided as a zipped file in the Supporting Information. To reduce the number of distinct atom types, and based on analysis of the DDEC-derived charges, we characterized atoms based on distinct chemical environments (Table 1 and Figure 2). We reserved one atom type for Al and two atom types for O, including O_b ions that connect Al and Si and O_z ions that connect two Si. The Si charge is sensitive to the number of neighboring AlO_4^- tetrahedra, leading to four distinct Si atom types. TMAda$^+$ C and H atoms are categorized based on their positions relative to the quaternary ammonium group. Atomic charges were derived by averaging over raw charges from the three configurations and imposing overall electroneutrality. The procedure was repeated on 10 additional relaxed DFT structures, and charges were found to vary by less than 5%. The relative energies are also insensitive to the partial charge variations, as two different partial charge sets only lead to a 1.0 kJ/mol$_{d6r}$ energy difference across tested configurations.

Table 1. Net Atomic Charges on Zeolite and TMAda$^+$ Atoms

molecule	atom type	$q(e)$	molecule	atom type	$q(e)$
CHA zeolite	Al	1.79584	TMAda$^+$	n	0.22348
	O_b[a]	−1.05771		cnh	−0.30327
	O_z[b]	−0.93365		hx	0.14625
	Si[c]	1.84506		cn	0.20907
	Si[d]	1.82378		cb	−0.27065
	Si[e]	1.8025		hb	0.10192
	Si[f]	1.78122		cj	0.05556
				hj	0.0712
				ce	−0.22186
				he	0.0907

[a] Oxygen bridging Al and Si. [b] Oxygen bridging two Si. [c] Si without the first-neighbor Al. [d] Si with one first-neighbor Al. [e] Si with two first-neighbor Al. [f] Si with three first-neighbor Al.

2.3. Classical Molecular Dynamics (CMD) Simulations. The LAMMPS[58] package was used to carry out all classical molecular dynamics (CMD) simulations. The cell parameters and locations of atoms, which were obtained from the Database of Zeolite Structures,[49] are the same as those used in AIMD simulations. Each simulation was equilibrated for 500 ps followed by a production run of 1500 ps, all using a time step of 0.2 fs. The production runs were divided into three sections, from which three block-averaged potential energies and their standard deviations were calculated to reflect the fluctuation of the energies. The NVT ensemble with the Nosé−Hoover[59,60] thermostat at 433 K was applied. A cutoff of 10 Å was used for nonbonded and electrostatic interactions. A standard long-range van der Waals tail correction was added to the energy and pressure, while a particle−particle particle-mesh solver[61] was used to describe the long-range electrostatics.

3. RESULTS AND DISCUSSION

3.1. Al Configurations and OSDA Orientations. We seek to explore the relationship between Al siting, TMAda$^+$ orientation, and system energy. To that end, we systematically enumerated all combinations of Al location and TMAda$^+$ orientations possible within a 36 T-site supercell containing three unique cages, shown in Figure 3. On the 100% siliceous framework, there are two symmetry-distinct orientations of TMAda$^+$ possible within the three cages of the supercell, shown in Figure 3 and labeled as "AAA" and "AAB" to indicate the relative orientations of the three TMAda$^+$. Onto this tableau, we distributed three Al over all available T-sites, excluding configurations that contain Al−O−Al linkages that violate Löwenstein's rule and that are not captured by the classical force field. This distribution process yields 4908 configurations per TMAda$^+$ orientation or a total of 9816 separate initial configurations that span (with some redundancy) all possibilities within the 36 T-site supercell. All structures are supplied in the Supporting Information. Si and Al are present in an 11/1 ratio in all supercells, a ratio dictated by the requirement to maintain charge neutrality within the system.

Molecular dynamics simulations were performed at 433 K on each of these 9816 configurations. Consistent with prior work,[43] TMAda$^+$ maintain their orientation throughout the simulation. Potential energy fluctuations, which were calculated from three block averages, during the MD simulations are less than 5 kJ/mol$_{d6r}$ after initial equilibrations of 500 ps. The average potential energy $\langle U\rangle_i$ of each configuration i was computed every 1000 timesteps, and the relative energy of each configuration ΔU_i was computed as

$$\Delta U_i = (\langle U\rangle_i - U_{ref})/N_{d6r} \qquad (1)$$

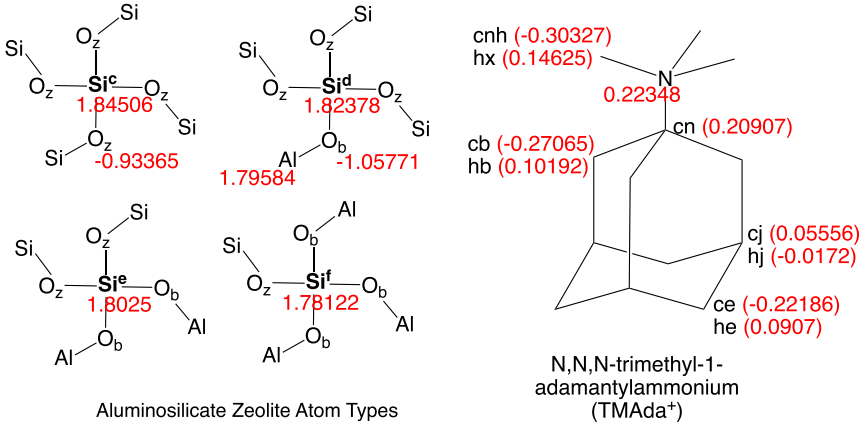

Figure 2. Structure of tetrahedra aluminosilicate unit, TMAda$^+$, and the definition of each atomic type used in Table 1. Atomic charges are labeled in red beside the atom types.

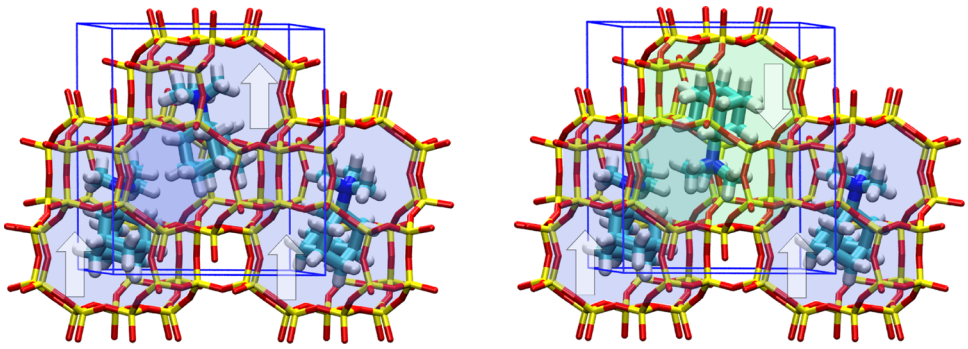

Figure 3. 36 T-site CHA supercell. Periodic cell boundaries are shown in blue, T-sites are shown in yellow, and oxygen is shown in red. The left and right images illustrate two unique (AAA and AAB) occlusions of $TMAda^+$; orientations are highlighted with blue or green shading of cha cages and with arrows.

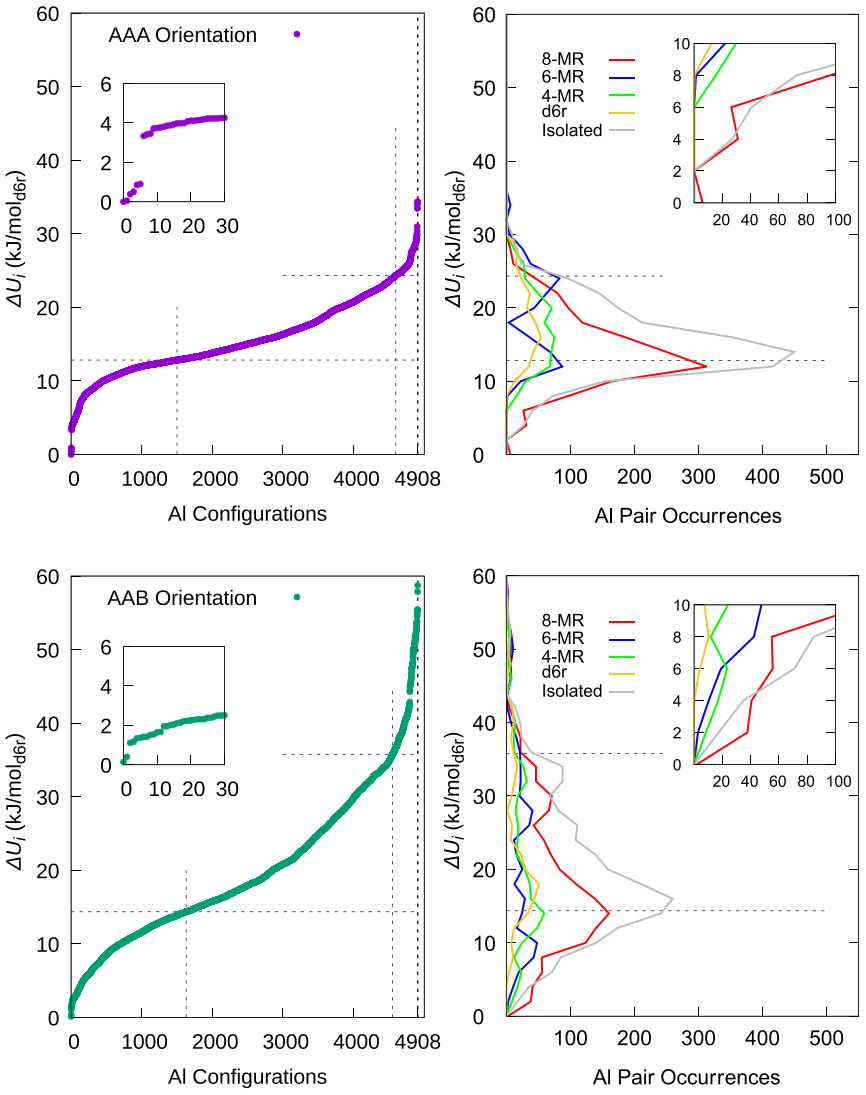

Figure 4. Mean potential energies (ΔU_i) of AAA configurations, sorted in ascending order (top left and inset); each dot represents the energy for an individual configuration. Histograms of Al−Al proximity features vs potential energy (top right and inset). The histogram bin size is 2.0 kJ/mol$_{d6r}$; consecutive bins are connected by straight lines. Corresponding results for AAB configurations are shown in the bottom left and right.

where the reference potential energy U_{ref} is taken as the lowest-energy configuration

$$U_{ref} = \min_i \{\langle U \rangle_i\} \quad (2)$$

and the energy is normalized by the number of d6r units. The left panels of Figure 4 report ΔU_i, sorted from lowest to highest energy, for the Al configurations in a field of AAA- and AAB-oriented $TMAda^+$, respectively. Several observations are immediately evident. First, energies span nearly 40 and 60 kJ/

https://doi.org/10.1021/acs.chemmater.2c01465
Chem. Mater. XXXX, XXX, XXX−XXX

mol_{d6r} in the AAA and AAB data sets, respectively, reflecting a substantial sensitivity to Al configuration within a given field of $TMAda^+$ and different sensitivities to different fields. Second, the lowest-energy Al configurations in the AAA and AAB sets are of similar energy. And third, a small handful of configurations dominate the low-energy (and high-energy) regimes.

Before analyzing the relationship between configurations and energy, we tested classical model predictions against AIMD results. We chose the 10 lowest- and 10 highest-energy configurations from the AAA and AAB sets and augmented with a number of intermediate energy configurations to create a basket of 72 configurations. Initial structures were extracted from the last frame of the 2 ns CMD simulations (POSCARs available in the Supporting Information). AIMD simulations were run at 633 K for 10 ps and the last 7.5 ps of trajectory used to calculate the average potential energy. Uncertainties were taken as the standard deviation obtained from three equal length blocks from the trajectory. Figure 5 plots the mean CMD energies against the AIMD energies, color coding according to $TMAda^+$ orientation, and choosing the lowest-energy AIMD AAB configuration as a reference. The uncertainties in the AIMD and CMD energies span comparable ranges. Mean energies and uncertainties are listed in Table S1 in the Supporting Information.

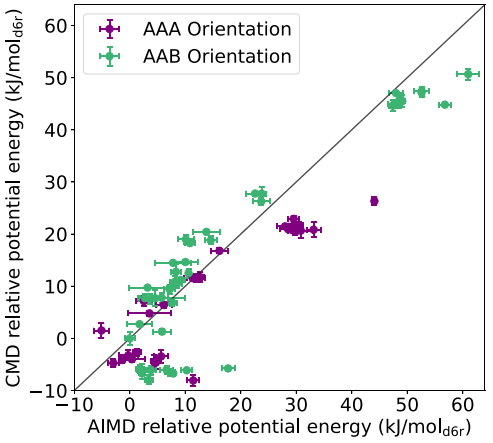

Figure 5. Parity plot of CMD potential energies against AIMD potential energies (per d6r unit). Purple and green dots correspond to AAA and AAB arrangements, respectively, and whiskers correspond to error estimates, as described in the text.

The energy range spanned by the AIMD results is consistent with the CMD-predicted spans and differences between the AAA and AAB subsets. Further, the best-fit line through the data has a correlation coefficient of 0.91, consistent with a robust correlation between the two models. Nonetheless, some substantial differences are evident. Within the envelope of low-energy structures, the AIMD energy variations are a factor of 4 greater than the CMD. Similar but smaller variations are evident in the higher-energy envelope. To characterize the origins of these differences, we used the minimum image convention and structure files to compute the three shortest Al−Al separations in a structure. In Figure S1 of the Supporting Information, we plot the difference between CMD and AIMD energies, $E_{CMD}-E_{AIMD}$, of the 20 lowest-CMD-energy structures against the average of the reciprocals of three Al−Al distances, motivated by the potential electrostatic origins of the discrepancies. The CMD and AIMD energy differences are obtained from data in Figure 5. Figure S1 shows that errors increase in absolute magnitude with decreasing Al−Al separations and in a fashion that is nearly linear in reciprocal separations. The CMD model thus overstabilizes structures that contain short Al−Al separations. Structures that contain mostly 2NN Al−Al pair features have the largest errors. These discrepancies represent limitations of the number of distinct atom types in the classical model. We conclude that the CMD model properly captures the larger energy variations in the system.

To explore the relationship between gross structure and energy, and in particular to look for the signatures of an electrostatic contribution to the large energy spans seen in Figure 4, we created parity plots of relative potential energies against ensemble-averaged $1/r_{N-N}$ (Supporting Information, Figure S2), $1/r_{Al-Al}$ (Supporting Information, Figure S3), and $1/r_{Al-N}$ (Figure 6) across all AAA and AAB configurations. Averages here are over the three shortest minimum image

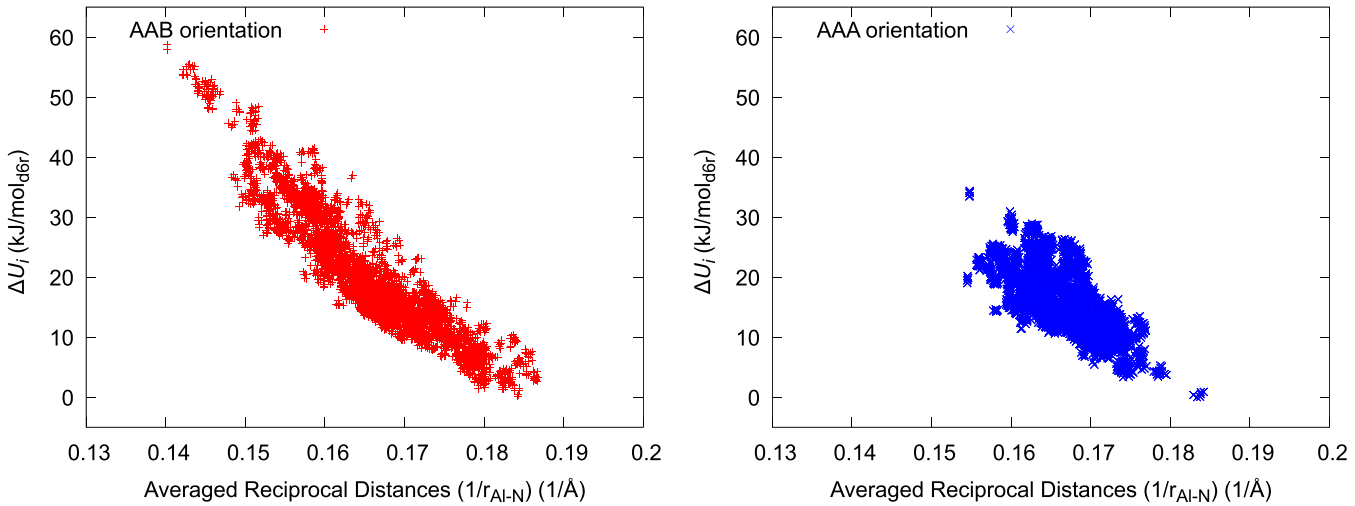

Figure 6. Relative potential energies (ΔU_i) vs reciprocal Al to quaternary ammonium N distances ($1/r_{Al-N}$) across Al configurations in a field of AAB (left) and AAA (right) $TMAda^+$.

https://doi.org/10.1021/acs.chemmater.2c01465
Chem. Mater. XXXX, XXX, XXX−XXX

distances, which capture the leading electrostatic contributions of each pair-wise interaction. ΔU_i is essentially uncorrelated with $1/r_{N-N}$ and $1/r_{Al-Al}$. In contrast, and as seen in Figure 6, energy and $1/r_{Al-N}$ are anticorrelated, so that configurations with lower mean reciprocal Al−N distances are generally lower in energy. The energy span is larger and correlation clearer for the AAB orientation (Figure 6, left) than for the AAA. The AAA and AAB orientations produce different distributions of Al−N separations. As shown in Figure 6, the AAB configuration both generates a higher density of configurations with larger mean reciprocal Al−N distances, corresponding to the greater density of low-energy configurations and a large number of configurations with mean Al−N distances much smaller than those accessible in the AAA configuration. The results suggest that the ability of cationic quaternary N centers to form close contacts with Al-substituted T-sites is a leading, although not sole, contributor to the potential energy differences and that those close contacts are more common in the AAA than in the AAB orientation of $TMAda^+$.

3.2. Al Ordering Analysis. We next explored the relationship between energy and Al configuration in the AAA $TMAda^+$ subset. As shown in the top left panel in Figure 4, configurations span relative energies between 0 and 40 kJ/mol_{d6r}, with a large density of configurations in the intermediate energy regime and sharper variations at the two extremes. By construction, the points include symmetry redundant configurations; for example, by inspection, the six lowest-energy configurations are symmetry-equivalent realizations of the same structure. The energy spread of less than 2 kJ/mol_{d6r} is within the threshold of energy fluctuation within the block-average sampling method.

To fingerprint each configuration, we identified the three shortest Al−Al contacts and classified each Al−Al contact either as one of the features shown in Figure 7 or as an isolated pair feature, i.e., two Al that do not share a ring and are too remote to charge-compensate a divalent ion. The right panel of Figure 4 reports histograms of these pair feature types vs energy in 2.0 kJ/mol_{d6r} wide bins, with histogram points plotted at the low-energy side of the bin. The areas beneath each histogram reflect the relative probabilities of each pair type using the 36 T-site configuration construction algorithm and the assumed 11/1 Si/Al ratio. Isolated pairs are statistically most common, followed by 8MR. Generally, in the low-energy region, configurations are rich in 8MR and isolated pairs and poor in 4MR and 6MR pairs. In contrast, high-energy configurations contain a mix of features, with 6MR slightly more prominent at the highest energies. Figure 8 shows five nondegenerate representative low- and five nondegenerate representative high-energy Al configurations from the AAA set. All five low-energy Al configurations have Al pairs on an 8MR, while the five high-energy Al configurations have Al pairs on the d6r unit, 6MR or 4MR. This placement on the 8MR appears to maximize the close contact with the quaternary ammonium center of $TMAda^+$. AIMD results agree with CMD predictions of the large energy difference between the low- and high-energy Al configurations. AIMD and CMD predictions do not agree on the precise identity of the lowest-energy configuration. Among all AIMD-computed configurations, AIMD predicts a configuration that contains only isolated Al as the lowest average potential energy (2.0 kJ/mol_{d6r} lower in energy than the lowest-energy configuration in structures 1−5 of Figure 8). AIMD and CMD predict the same highest-energy configuration (structure 10 of Figure 8).

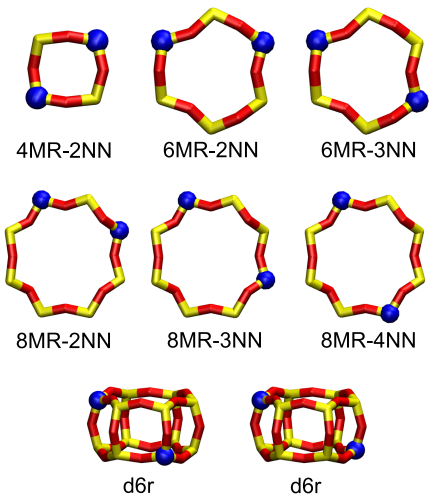

Figure 7. Al−Al pair proximity features in the CHA zeolite framework. All other pair features are categorized as isolated.

To uncover patterns in energy vs features, we separated the configurations into three subsets by fitting the energy vs configuration data to two third-order polynomials across the first and second halves of the profile and partitioning at the two inflection points. This partitioning resulted in 1499, 3098, and 311 configurations in the low-, medium-, and high-energy bins. We then Boltzmann-weighted the configurations within each bin, arbitrarily choosing 433 K because it is representative of typical zeolite synthesis conditions. The RT at 433 K is 3.6 kJ/mol, so that averaging captures significant fractions of each bin. The configurational integral of the system with the AAA $TMAda^+$ orientation is

$$Z^{AAA} = \sum_i e^{-\Delta U_i/kT} \tag{3}$$

where i denotes an Al configuration, ΔU_i is defined by eq 1, k is the Boltzmann constant, T is the averaging temperature, and only AAA orientations are considered in the summation. The probability of an Al configuration i with an AAA $TMAda^+$ orientation is

$$P_i = \frac{e^{-\Delta U_i/kT}}{Z^{AAA}} \tag{4}$$

Finally, the probability Π_j of a particular Al pair feature j is

$$\Pi_j = \sum_i \frac{n_{j,i}}{3} P_i \tag{5}$$

where the $n_{j,i}$ stands for the number of Al pair feature types j in Al configuration i. A factor of 3 accounts for the fact that there are three Al pair features in each configuration.

Figure 9 compares the probabilities of Al pair feature types within each energy bin with that expected from a random distribution of Al subject to Löwenstein's rule, corresponding to the integral of the histograms in Figure 4. Within this random distribution, the most probable Al pair types are 8MR and isolated, with a relatively small population of 6MR. The low-energy bin is similarly dominated by 8MR and isolated features; further, the 6MR and 4MR Al pair features occur at a very low probability. Those 6MR pair features, in contrast, are

https://doi.org/10.1021/acs.chemmater.2c01465
Chem. Mater. XXXX, XXX, XXX−XXX

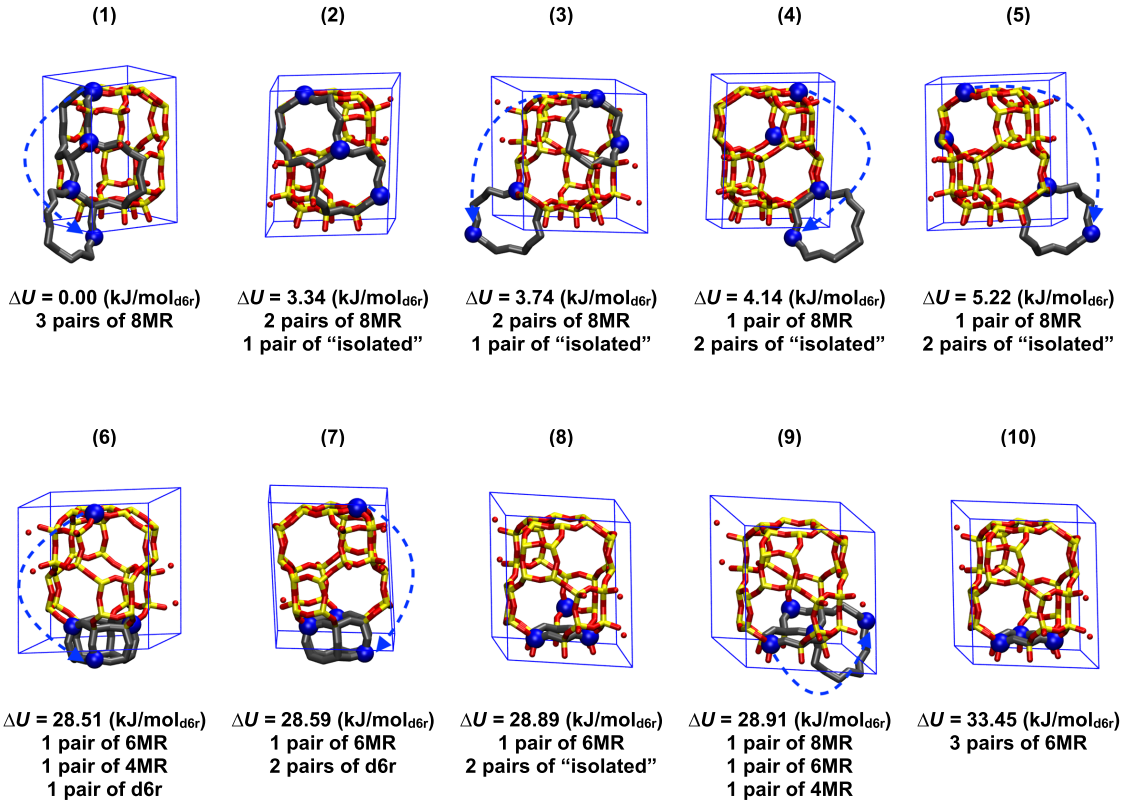

Figure 8. Lowest-energy (1−5) and highest-energy (6−10) AAA CMD supercells and corresponding Al pair features. Features within the supercell are highlighted in gray, and features across cell boundary are indicated with blue dashed arrows. Color: blue, Al; yellow, Si; and red, O.

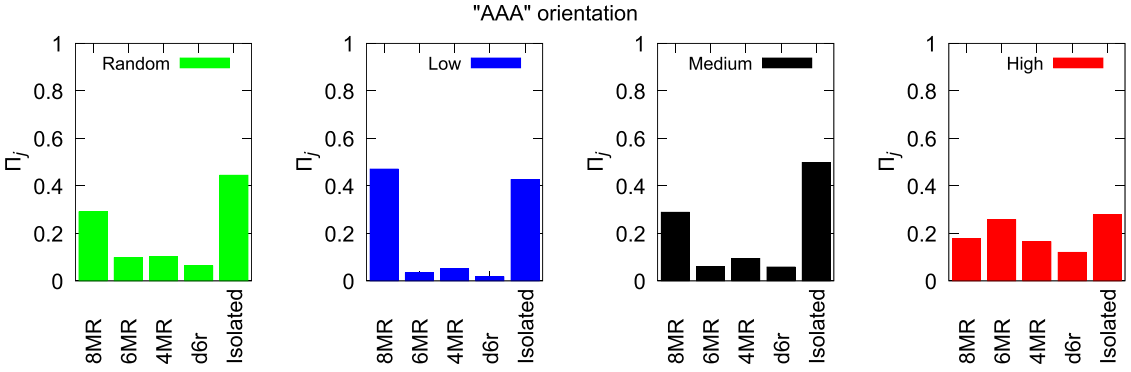

Figure 9. Probability distributions (Π_j) of the AAA TMAda$^+$ orientations. The left panel (green) represents the random Al distribution with Löwenstein's rule. "Low" (blue), "middle" (black), and "high" (red) distributions are from Boltzmann weightings over configurations subpartitioned by relative energy.

common in the high-energy bin. Results are consistent with the AAA orientation of TMAda$^+$ biasing against Al close contacts.

The bottom left panel in Figure 4 reports the mean potential energies of the AAB configurations, plotted using the same reference energy as that for the AAA configurations. Lowest-energy configurations are of similar energy, but AAB energies span 60 kJ/mol$_{d6r}$, exceeding the AAA span by more than 20 kJ/mol$_{d6r}$. The bottom right panel in Figure 4 shows the corresponding Al−Al feature histogram. 6MR, 4MR, and d6r Al pairs are represented more prominently at low energy in the AAB orientation than in AAA.

Figure 10 shows snapshots of five lowest- and five highest-energy AAB configurations, while Figure 11 shows the probabilities of Al pair types for the AAB orientation, calculated using the same strategy as described above for the AAA orientation (1629, 2920, and 359 Al configurations for low-energy, medium-energy, and high-energy regions, respectively). Similar to the AAA orientation, all five low-energy snapshots have 8MR Al pair features and most of these also have isolated Al pair features. However, in the AAB orientation, two of the low-energy configurations also contain 4MR pair features. The five high-energy configurations all contain 6MR Al pair features, as observed in the AAA orientation. As with the AAA orientation, AIMD and CMD predictions for AAB agree in terms of gross energy differences but differ in terms of the lowest-energy structures. Among all AIMD-computed configurations, AIMD predicts a configuration that contains only isolated Al to have the lowest average potential energy (2.0 kJ/mol$_{d6r}$ lower in energy than the lowest-energy configuration in structures 1−5 of Figure 10).

https://doi.org/10.1021/acs.chemmater.2c01465
Chem. Mater. XXXX, XXX, XXX−XXX

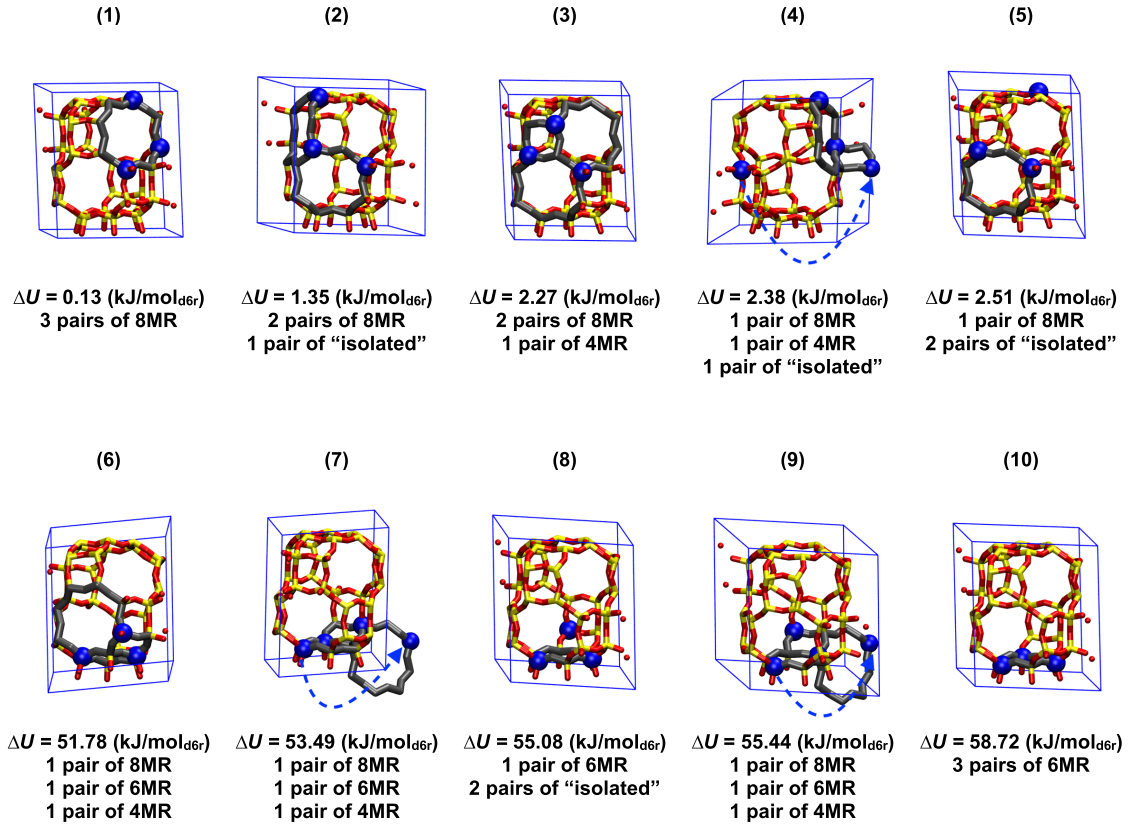

Figure 10. Lowest-energy (1−5) and highest-energy (6−10) AAB CMD supercells and corresponding Al pair features. Features within the supercell are highlighted in gray, and features across cell boundary are indicated with blue dashed arrows. Color: blue, Al; yellow, Si; and red, O.

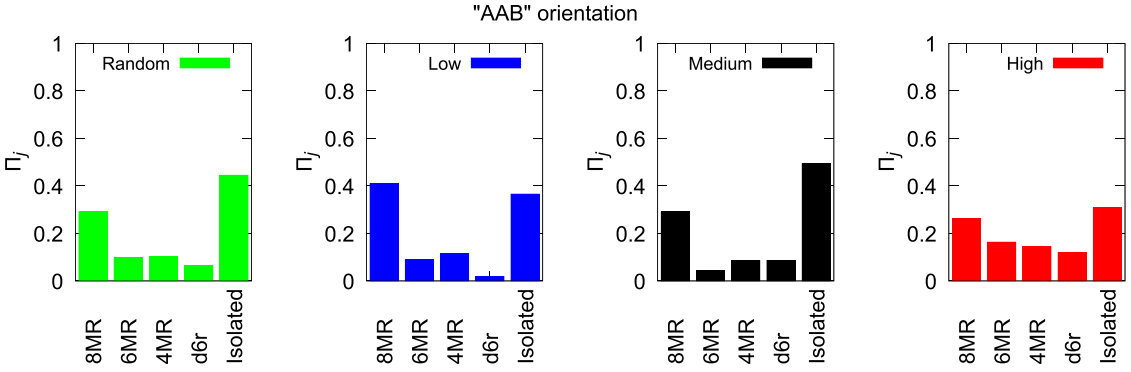

Figure 11. Probability distributions (Π_j) of the AAB TMAda$^+$ orientations. The left panel (green) represents the random Al distribution with Löwenstein's rule. Low (blue), middle (black), and high (red) distributions are from Boltzmann weightings over configurations subpartitioned by relative energy.

AIMD and CMD predict the same highest-energy configuration (structure 10 of Figure 10).

Figure 11 shows the Al pair feature probabilities computed at 433 K for the AAB orientation. Overall, the probability distribution is similar to the AAA orientation. Frameworks are predicted to be enriched in 8MR pairs relative to a random distribution and to have a large fraction of isolated pairs. The probability of 6MR and 4MR pairs, however, is comparable to the random distribution and considerably greater than the probability in the AAA orientation. Al pair distributions are thus sensitive to TMAda$^+$ relative ordering, suggesting a strategy for controlling that distribution. CHA zeolites crystallized with TMAda$^+$ as the sole SDA, with no additional Na$^+$, are observed to be poor in 6MR Al pairs,[11,34,38] consistent with a large manifold of low-energy AAA configurations and the lowest-energy AAB configurations.

To further explore the sensitivity of potential energy to TMAda$^+$ orientation, we selected the lowest-energy Al configurations from the AAA set, which contains only 8MR pairs, flipped the orientations of each TMAda$^+$ to create eight OSDA orientations, and computed the averaged potential energies. Results are shown in Figure 12, top. Flipping OSDAs within the low-energy configuration results in a number of degenerate structures due to system symmetry. The energy cost to flip TMAda$^+$ is modest (10 kJ/mo$_{d6r}$) and essentially constant—this 8MR-only structure, which avoids 6MR pairs, is relatively robust to OSDA orientation. We applied the same strategy to an Al configuration that contains 6MR and d6r

https://doi.org/10.1021/acs.chemmater.2c01465
Chem. Mater. XXXX, XXX, XXX−XXX

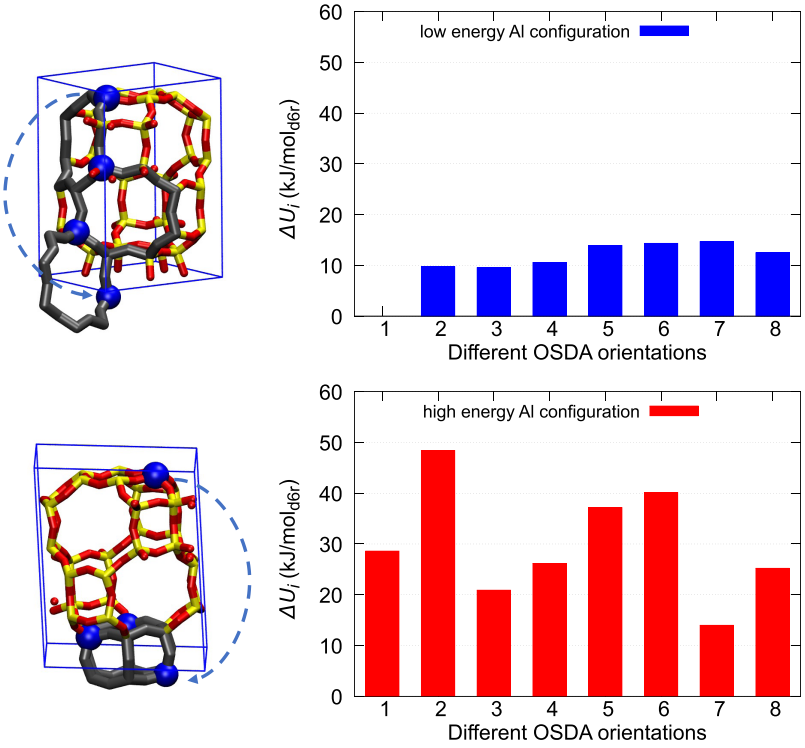

Figure 12. Mean potential energies of an 8MR-pair-only configuration (top) and a configuration containing 6MR and d6r pairs (bottom), each in the field of all possible TMAda$^+$ orientations. Al T-sites highlighted in blue and arrows indicate periodic images.

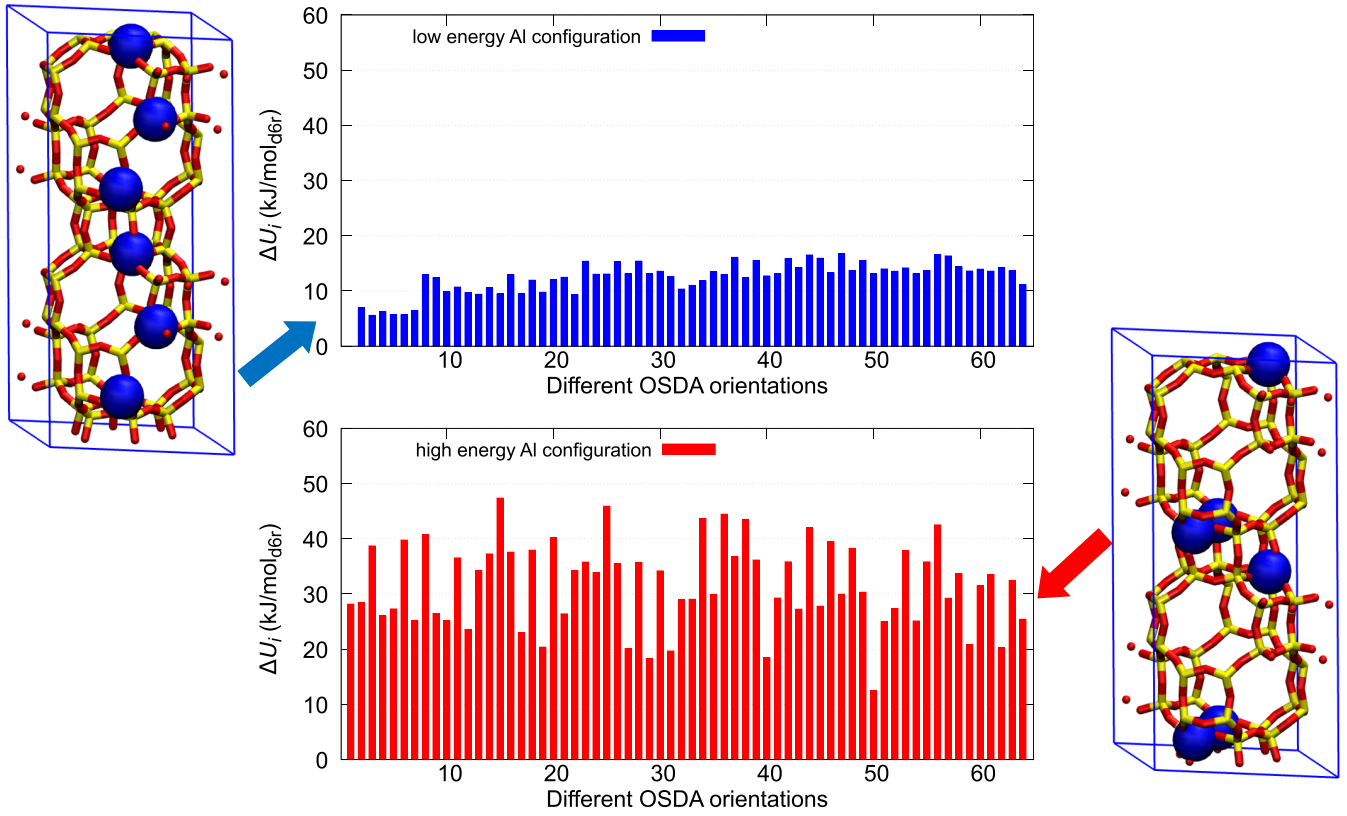

Figure 13. Mean potential energies of a 72-T-site 8MR-pair-only configuration (top) and a 72-T-site configuration containing 6MR and d6r pair features (bottom), each in the field of all possible TMAda$^+$ orientations. The same OSDA orientation with different Al configurations is stacked. Al T-sites are highlighted in blue.

pairs. As shown in the bottom of Figure 12, the energy of this configuration is highly sensitive to TMAda$^+$ orientation. While its lowest-energy realization is competitive in energy with the 8MR-only structure, most orientations lead to much higher

https://doi.org/10.1021/acs.chemmater.2c01465
Chem. Mater. XXXX, XXX, XXX−XXX

energies. These results suggest that some features, such as the 8MR pair, may be preferentially biased for because they are agnostic to local OSDA orientation, while others, such as the 6MR pair, are biased against because they are more sensitive to local OSDA orientation.

We doubled the supercells shown in Figure 12 along the *c* direction and repeated the $TMAda^+$ flipping procedure, creating 64 OSDA orientational combinations per supercell. Supercells and mean potential energies are shown in Figure 13. The results mirror those of Figure 12: the 8MR-only Al configuration is minimized in energy when all $TMAda^+$ are aligned in the same orientation ("AAAAAA") but energy costs to "flip" OSDA are relatively small and constant. In contrast, the 6MR Al configuration is higher in energy across all configurations save number 50; further, energies are much more sensitive to $TMAda^+$ orientations.

4. CONCLUSIONS

While the ability to guide zeolite structures through OSDA selection, and approaches to simulate this influence, is well established, the relationship between OSDA choice and the distribution of Al on a zeolite framework is less clear. CHA is an ideal template for exploring these effects, as it has only one symmetry-distinct T-site; all T-sites thus see identical void environments within the framework, and nonrandom Al distributions must reflect either kinetic or thermodynamic factors at play during crystallization. Here, we explore the thermodynamics of Al distributions in the field of $TMAda^+$ structure directing agents, using a combination of *ab initio* and classical dynamics models of $TMAda^+$ occluded within the three cages of a CHA unit cell. System energies are observed to be sensitive both to Al proximity and to the field of $TMAda^+$, and energy variations are consistent with a substantial contribution from OSDA-Al electrostatics, related to the ability of quaternary nitrogen to approach Al T-sites. Configurations that place Al pairs in 8MRs maximize favorable electrostatic contacts with $TMAda^+$ and are low in energy. Further, the energies of those configurations are less sensitive to $TMAda^+$ orientation than are Al pairs in smaller rings. This robustness to OSDA order (or disorder) may thus be a relevant factor in determining Al distributions. Al configurations that place two Al within the same 6MR are high in energy, consistent with experimental observations that these features are rare on CHA zeolite prepared with $TMAda^+$ as the sole structure directing agent.[34,35] This correspondence suggests that lattice energies are, at least in this system, a useful predictor of Al siting preferences, as has been observed in similar simulations exploring the influence of Na^+ and $TMAda^+$ co-occlusion on Al siting.[36]

The results highlight the potential to apply similar strategies to other OSDAs and frameworks. The CHA−$TMAda^+$ system is simplified by the fact that $TMAda^+$ can adopt only one of two primary orientations within the cha cage, and models here are limited to Al as the sole charge-carrying site on the framework. Further extensions will benefit from improvements in force field parameterization, in configurational sampling, and in model generalizations to framework compositions away from 1:1 OSDA to Al and thus to Si/Al ratios away from 11/1.

■ ASSOCIATED CONTENT

Supporting Information

The Supporting Information is available free of charge at https://pubs.acs.org/doi/10.1021/acs.chemmater.2c01465.

CMD, AIMD energies, and uncertainties plotted in Figure 5; analysis of data scattering in Figure 5; analysis of the correlations of the Al−Al distance and N−N distance with the relative potential energy (ΔU_i); VASP input files for geometry optimization, charge generation, and AIMD simulations; LAMMPS input file for CMD simulations; XYZ files for all CMD simulations; CONTCARs of DFT-optimized structures used for charge analysis and corresponding XYZ files that contain raw partial charges; POSCARs of 72 structures that are used for the analysis of CMD and AIMD correlations; and TXT files containing raw data that is used to plot figures (PDF)

■ AUTHOR INFORMATION

Corresponding Author

William F. Schneider − *Department of Chemical and Biomolecular Engineering, University of Notre Dame, Notre Dame, Indiana 46556, United States; Department of Chemistry and Biochemsitry, University of Notre Dame, Notre Dame, Indiana 46556, United States;* orcid.org/0000-0003-0664-2138; Email: wschneider@nd.edu

Authors

Xiaoyu Wang − *Department of Chemical and Biomolecular Engineering, University of Notre Dame, Notre Dame, Indiana 46556, United States;* orcid.org/0000-0003-2228-0114

Yujia Wang − *Department of Chemistry and Biochemistry, University of Notre Dame, Notre Dame, Indiana 46556, United States;* orcid.org/0000-0002-6715-4114

Ahmad Moini − *BASF Corporation, Iselin, New Jersey 08830, United States*

Rajamani Gounder − *Charles D. Davidson School of Chemical Engineering, Purdue University, West Lafayette, Indiana 47907, United States;* orcid.org/0000-0003-1347-534X

Edward J. Maginn − *Department of Chemical and Biomolecular Engineering, University of Notre Dame, Notre Dame, Indiana 46556, United States;* orcid.org/0000-0002-6309-1347

Complete contact information is available at: https://pubs.acs.org/10.1021/acs.chemmater.2c01465

Notes

The authors declare no competing financial interest.

■ ACKNOWLEDGMENTS

The authors gratefully acknowledge financial support from the National Science Foundation CBET-DMREF program under award number 1922154. The computing resources for this work were provided by the Notre Dame Center for Research Computing.

■ REFERENCES

(1) Corma, A. State of the art and future challenges of zeolites as catalysts. *J. Catal.* **2003**, *216*, 298−312.

(2) Moliner, M.; Rey, F.; Corma, A. Towards the rational design of efficient organic structure-directing agents for zeolite synthesis. *Angew. Chem., Int. Ed.* **2013**, *52*, 13880−13889.

(3) Gómez-Hortigüela, L.; Camblor, M. A. *Insights into the Chemistry of Organic Structure-Directing Agents in the Synthesis of Zeolitic Materials*; Springer, 2017; pp 1−41.

(4) Pophale, R.; Daeyaert, F.; Deem, M. W. Computational Prediction of Chemically Synthesizable Organic Structure Directing Agents for Zeolites. *J. Mater. Chem. A* **2013**, *1*, 6750−6760.
(5) Schmidt, J. E.; Deem, M. W.; Davis, M. E. Synthesis of a Specified, Silica Molecular Sieve by Using Computationally Predicted Organic Structure-Directing Agents. *Angew. Chem., Int. Ed.* **2014**, *126*, 8512−8514.
(6) Davis, T. M.; Liu, A. T.; Lew, C. M.; Xie, D.; Benin, A. I.; Elomari, S.; Zones, S. I.; Deem, M. W. Computationally Guided Synthesis of SSZ-52: A Zeolite for Engine Exhaust Clean-Up. *Chem. Mater.* **2016**, *28*, 708−711.
(7) Deem, M. W.; Pophale, R.; Cheeseman, P. A.; Earl, D. Computational discovery of new zeolite-like materials. *J. Phys. Chem. C* **2009**, *113*, 21353−21360.
(8) Boal, B. W.; Deem, M. W.; Xie, D.; Kang, J. H.; Davis, M. E.; Zones, S. I. Synthesis of germanosilicate molecular sieves from mono- and di-quaternary ammonium OSDAs constructed from benzyl imidazolium derivatives: Stabilization of large micropore volumes including new molecular sieve CIT-13. *Chem. Mater.* **2016**, *28*, 2158−2164.
(9) Gallego, E. M.; Portilla, M. T.; Paris, C.; León-Escamilla, A.; Boronat, M.; Moliner, M.; Corma, A. "Ab initio" synthesis of zeolites for preestablished catalytic reactions. *Science* **2017**, *355*, 1051−1054.
(10) Haag, W. O.; Lago, R.; Weisz, P. The active site of acidic aluminosilicate catalysts. *Nature* **1984**, *309*, 589−591.
(11) Kester, P. M.; Crum, J. T.; Li, S.; Schneider, W. F.; Gounder, R. Effects of Brønsted acid site proximity in chabazite zeolites on OH infrared spectra and protolytic propane cracking kinetics. *J. Catal.* **2021**, *395*, 210−226.
(12) Chen, G.; Liu, H.; Fadaeerayeni, S.; Shan, J.; Xing, A.; Cheng, J.; Wang, H.; Xiang, Y. Tuning the reactivity of ethylene oligomerization by HZSM-5 framework Al_f proximity. *Catal. Sci. Technol.* **2020**, *10*, 4019−4029.
(13) Nystrom, S.; Hoffman, A.; Hibbitts, D. Tuning Brønsted acid strength by altering site proximity in CHA framework zeolites. *Catal. Sci. Technol.* **2018**, *8*, 7842−7860.
(14) Bhan, A.; Iglesia, E. A link between reactivity and local structure in acid catalysis on zeolites. *Acc. Chem. Res.* **2008**, *41*, 559−567.
(15) Román-Leshkov, Y.; Moliner, M.; Davis, M. E. Impact of controlling the site distribution of Al atoms on catalytic properties in ferrierite-type zeolites. *J. Phys. Chem. C* **2011**, *115*, 1096−1102.
(16) Dedecek, J.; Wichterlova, B. Siting and redox behavior of Cu ions in CuH-ZSM-5 zeolites. Cu^+ photoluminescence study. *J. Phys. Chem. A* **1994**, *98*, 5721−5727.
(17) Dedecek, J.; Sobalik, Z.; Tvaruazkova, Z.; Kaucky, D.; Wichterlova, B. Coordination of Cu ions in high-silica zeolite matrixes. Cu^+ photoluminescence, IR of NO adsorbed on Cu^{2+}, and Cu^{2+} ESR study. *J. Phys. Chem. B* **1995**, *99*, 16327−16337.
(18) Walspurger, S.; Louis, B. Insights into the structure of active sites in metal-doped solid acid catalysts. *Appl. Catal., A* **2008**, *336*, 109−115.
(19) Giordanino, F.; Vennestrøm, P. N. R.; Lundegaard, L. F.; Stappen, F. N.; Mossin, S.; Beato, P.; Bordiga, S.; Lamberti, C. Characterization of Cu-exchanged SSZ-13: a comparative FTIR, UV-Vis, and EPR study with Cu-ZSM-5 and Cu-β with similar Si/Al and Cu/Al ratios. *Dalton Trans.* **2013**, *42*, No. 12741.
(20) Paolucci, C.; Parekh, A. A.; Khurana, I.; Di Iorio, J. R.; Li, H.; Albarracin Caballero, J. D.; Shih, A. J.; Anggara, T.; Delgass, W. N.; Miller, J. T.; et al. Catalysis in a Cage: Condition-Dependent Speciation and Dynamics of Exchanged Cu Cations in SSZ-13 Zeolites. *J. Am. Chem. Soc.* **2016**, *138*, 6028−6048.
(21) Li, S.; Wang, Y.; Wu, T.; Schneider, W. F. First-principles analysis of site-and condition-dependent Fe speciation in SSZ-13 and implications for catalyst optimization. *ACS Catal.* **2018**, *8*, 10119−10130.
(22) Li, H.; Paolucci, C.; Khurana, I.; Wilcox, L.; Göltl, F.; Albarracin-Caballero, J. D.; Shih, A. J.; Ribeiro, F. H.; Gounder, R.; Schneider, W. F. Consequences of exchange-site heterogeneity and dynamics on the UV−visible spectrum of Cu-exchanged SSZ-13. *Chem. Sci.* **2019**, *10*, 2373−2384.
(23) Devos, J.; Bols, M. L.; Plessers, D.; Goethem, C. V.; Seo, J. W.; Hwang, S.-J.; Sels, B. F.; Dusselier, M. Synthesis−structure−activity relations in Fe-CHA for C-H activation: control of Al distribution by interzeolite conversion. *Chem. Mater.* **2020**, *32*, 273−285.
(24) Knott, B. C.; Nimlos, C. T.; Robichaud, D. J.; Nimlos, M. R.; Kim, S.; Gounder, R. Consideration of the aluminum distribution in zeolites in theoretical and experimental catalysis research. *ACS Catal.* **2018**, *8*, 770−784.
(25) Yokoi, T.; Mochizuki, H.; Namba, S.; Kondo, J. N.; Tatsumi, T. Control of the Al distribution in the framework of ZSM-5 zeolite and its evaluation by solid-state NMR technique and catalytic properties. *J. Phys. Chem. C* **2015**, *119*, 15303−15315.
(26) Pashkova, V.; Klein, P.; Dedecek, J.; Tokarová, V.; Wichterlová, B. Incorporation of Al at ZSM-5 hydrothermal synthesis. Tuning of Al pairs in the framework. *Microporous Mesoporous Mater.* **2015**, *202*, 138−146.
(27) Biligetu, T.; Wang, Y.; Nishitoba, T.; Otomo, R.; Park, S.; Mochizuki, H.; Kondo, J. N.; Tatsumi, T.; Yokoi, T. Al distribution and catalytic performance of ZSM-5 zeolites synthesized with various alcohols. *J. Catal.* **2017**, *353*, 1−10.
(28) Nimlos, C. T.; Hoffman, A. J.; Hur, Y. G.; Lee, B. J.; di Iorio, J. R.; Hibbitts, D. D.; Gounder, R. Experimental and theoretical assessments of aluminum proximity in MFI zeolites and its alteration by organic and inorganic structure-directing agents. *Chem. Mater.* **2020**, *32*, 9277−9298.
(29) Román-Leshkov, Y.; Moliner, M.; Davis, M. E. Impact of Controlling the Site Distribution of Al Atoms on Catalytic Properties in Ferrierite-Type Zeolites. *J. Phys. Chem. C* **2011**, *115*, 1096−1102.
(30) Pinar, A.; Márquez-Álvarez, C.; Grande-Casas, M.; Pérez-Pariente, J. Template-controlled acidity and catalytic activity of ferrierite crystals. *J. Catal.* **2009**, *263*, 258−265.
(31) Pinar, A. B.; Gómez-Hortigüela, L.; McCusker, L. B.; Perez-Pariente, J. Controlling the Aluminum Distribution in the Zeolite Ferrierite via the Organic Structure Directing Agent. *Chem. Mater.* **2013**, *25*, 3654−3661.
(32) Pinar, A. B.; Rzepka, P.; Knorpp, A. J.; McCusker, L. B.; Baerlocher, C.; Huthwelker, T.; van Bokhoven, J. A. Pinpointing and Quantifying the Aluminum Distribution in Zeolite Catalysts Using Anomalous Scattering at the Al Absorption Edge. *J. Am. Chem. Soc.* **2021**, *143*, 17926−17930.
(33) Muraoka, K.; Chaikittisilp, W.; Yanaba, Y.; Yoshikawa, T.; Okubo, T. Directing Aluminum Atoms into Energetically Favorable Tetrahedral Sites in a Zeolite Framework by Using Organic Structure-Directing Agents. *Angew. Chem., Int. Ed.* **2018**, *57*, 3742−3746.
(34) di Iorio, J. R.; Gounder, R. Controlling the Isolation and Pairing of Aluminum in Chabazite Zeolites Using Mixtures of Organic and Inorganic Structure-Directing Agents. *Chem. Mater.* **2016**, *28*, 2236−2247.
(35) di Iorio, J. R.; Nimlos, C. T.; Gounder, R. Introducing Catalytic Diversity Into Single-Site Chabazite Zeolites of Fixed Composition via Synthetic Control of Active Site Proximity. *ACS Catal.* **2017**, *7*, 6663−6674.
(36) Di Iorio, J. R.; di Iorio, J. R.; Li, S.; Jones, C. B.; Nimlos, C. T.; Wang, Y.; Kunkes, E.; Vattipalli, V.; Prasad, S.; Moini, A.; Schneider, W. F. Cooperative and Competitive Occlusion of Organic and Inorganic Structure-Directing Agents within Chabazite Zeolites Influences Their Aluminum Arrangement. *J. Am. Chem. Soc.* **2020**, *142*, 4807−4819.
(37) Zhang, J.; Shan, Y.; Zhang, L.; Du, J.; He, H.; Han, S.; Lei, C.; Wang, S.; Fan, W.; Feng, Z.; Liu, X.; Meng, X.; Xiao, F.-S. Importance of controllable Al sites in CHA framework by crystallization pathways for NH3-SCR reaction. *Appl. Catal., B* **2020**, *277*, No. 119193.
(38) Lee, S.; Nimlos, C. T.; Kipp, E. R.; Wang, Y.; Gao, X.; Schneider, W. F.; Lusardi, M.; Vattipalli, V.; Prasad, S.; Moini, A.; Gounder, R. Evolution of Framework Al Arrangements in CHA Zeolites during Crystallization in the Presence of Organic and

https://doi.org/10.1021/acs.chemmater.2c01465
Chem. Mater. XXXX, XXX, XXX−XXX

Inorganic Structure-Directing Agents. *Cryst. Growth Des.* **2022**, *22*, 6275−6295.
(39) Zones, S. I. Zeolite SSZ-13 and Its Method of Preparation. U.S. Patent US4,544,5381985.
(40) Fletcher, R. E.; Ling, S.; Slater, B. Violations of Löwenstein's Rule in Zeolites. *Chem. Sci.* **2017**, *8*, 7483−7491.
(41) Li, S.; Li, H.; Gounder, R.; Debellis, A.; et al. First-principles comparison of proton and divalent copper cation exchange energy landscapes in SSZ-13 zeolite. *J. Phys. Chem. C* **2018**, *122*, 23564−23573.
(42) Tang, X.; Liu, Z.; Huang, L.; Chen, W.; Li, C.; Wang, G.; Li, G.; Yi, X.; Zheng, A. Violation or Abidance of Löwenstein's Rule in Zeolites Under Synthesis Conditions? *ACS Catal.* **2019**, *9*, 10618−10625.
(43) Li, S.; Gounder, R.; Debellis, A.; et al. Influence of the N, N, N-Trimethyl-1-adamantyl Ammonium Structure-Directing Agent on Al Substitution in SSZ-13 Zeolite. *J. Phys. Chem. C* **2019**, *123*, 17454−17458.
(44) Loewenstein, W. The distribution of aluminum in the tetrahedra of silicates and aluminates. *Am. Mineral.* **1954**, *39*, 92−96.
(45) Gallego, E. M.; Li, C.; Paris, C.; Martín, N.; Martínez-Triguero, J.; Boronat, M.; Moliner, M.; Corma, A. Making Nanosized CHA Zeolites with Controlled Al Distribution for Optimizing Methanol-to-Olefin Performance. *Chem. - Eur. J.* **2018**, *24*, 14631−14635.
(46) Schwalbe-Koda, D.; Kwon, S.; Paris, C.; Bello-Jurado, E.; Jensen, Z.; Olivetti, E.; Willhammar, T.; Corma, A.; Román-Leshkov, Y.; Moliner, M.; Gómez-Bombarelli, R. A priori control of zeolite phase competition and intergrowth with high-throughput simulations. *Science* **2021**, *374*, 308−315.
(47) Mayo, S. L.; Olafson, B. D.; Goddard, W. A. DREIDING: a generic force field for molecular simulations. *J. Phys. Chem. C* **1990**, *94*, 8897−8909.
(48) Kresse, G.; Furthmüller, J. Efficient iterative schemes for ab initio total-energy calculations using a plane-wave basis set. *Phys. Rev. B* **1996**, *54*, 11169−11186.
(49) Baerlocher, C.; McCusker, L. Database of Zeolite Structures, 2022. http://www.iza-structure.org/databases/.
(50) Blöchl, P. E. Projector augmented-wave method. *Phys. Rev. B* **1994**, *50*, 17953−17979.
(51) Kresse, G.; Joubert, D. From ultrasoft pseudopotentials to the projector augmented-wave method. *Phys. Rev. B* **1999**, *59*, 1758−1775.
(52) Perdew, J. P.; Wang, Y. Accurate and simple analytic representation of the electron-gas correlation energy. *Phys. Rev. B* **1992**, *45*, 13244−13249.
(53) Grimme, S.; Antony, J.; Ehrlich, S.; Krieg, H. A consistent and accurate ab initio parametrization of density functional dispersion correction (DFT-D) for the 94 elements H-Pu. *J. Chem. Phys.* **2010**, *132*, No. 154104.
(54) Manz, T. A. USER'S GUIDE Chargemol Program for Performing DDEC Atomic Population Analysis, 2022. https://sourceforge.net/projects/ddec//.
(55) Manz, T. A.; Sholl, D. S. Chemically meaningful atomic charges that reproduce the electrostatic potential in periodic and nonperiodic materials. *J. Chem. Theory Comput.* **2010**, *6*, 2455−2468.
(56) Manz, T. A.; Sholl, D. S. Improved atoms-in-molecule charge partitioning functional for simultaneously reproducing the electrostatic potential and chemical states in periodic and nonperiodic materials. *J. Chem. Theory Comput.* **2012**, *8*, 2844−2867.
(57) Manz, T. A.; Limas, N. G. Introducing DDEC6 atomic population analysis: part 1. Charge partitioning theory and methodology. *RSC Adv.* **2016**, *6*, 47771−47801.
(58) Plimpton, S. Fast parallel algorithms for short-range molecular dynamics. *J. Comput. Phys.* **1995**, *117*, 1−19.
(59) Nosé, S. A unified formulation of the constant temperature molecular dynamics methods. *J. Chem. Phys.* **1984**, *81*, 511−519.
(60) Hoover, W. G. Canonical dynamics: Equilibrium phase-space distributions. *Phys. Rev. A* **1985**, *31*, 1695.
(61) Hockney, R. W.; Eastwood, J. W. *Computer Simulation Using Particles*; CRC Press, 2021.

https://doi.org/10.1021/acs.chemmater.2c01465
Chem. Mater. XXXX, XXX, XXX−XXX